Eye-Specific IOP-Induced Displacements and Deformations of Human Lamina Cribrosa

Ian A. Sigal,[1–3] Jonathan L. Grimm,[1] Ning-Jiun Jan,[1,2] Korey Reid,[4] Don S. Minckler,[4] and Donald J. Brown[4]

[1]Department of Ophthalmology, UPMC Eye Center, Ophthalmology and Visual Science Research Center, University of Pittsburgh School of Medicine, Pittsburgh, Pennsylvania
[2]Department of Bioengineering, Swanson School of Engineering, University of Pittsburgh, Pittsburgh, Pennsylvania
[3]McGowan Institute for Regenerative Science, University of Pittsburgh School of Medicine, Pittsburgh, Pennsylvania
[4]Gavin Herbert Eye Institute, University of California, Irvine, Irvine, California

Correspondence: Ian A. Sigal, Ocular Biomechanics Laboratory, Department of Ophthalmology, University of Pittsburgh Medical Center, Eye & Ear Institute, 203 Lothrop Street, Rm. 930, Pittsburgh, PA 15213; sigalia@upmc.edu.

Submitted: July 2, 2013
Accepted: November 22, 2013

Citation: Sigal IA, Grimm JL, Jan N-J, et al. Eye-specific IOP-induced displacements and deformations of human lamina cribrosa. *Invest Ophthalmol Vis Sci*. 2014;55:1–15. DOI:10.1167/iovs.13–12724

Purpose. To measure high-resolution eye-specific displacements and deformations induced within the human LC microstructure by an acute increase in IOP.

Methods. Six eyes from donors aged 23 to 82 were scanned using second harmonic-generated (SHG) imaging at various levels of IOP from 10 to 50 mm Hg. An image registration technique was developed, tested, and used to find the deformation mapping between maximum intensity projection images acquired at low and elevated IOP. The mappings were analyzed to determine the magnitude and distribution of the IOP-induced displacements and deformations and contralateral similarity.

Results. Images of the LC were obtained and the registration technique was successful. IOP increases produced substantial, and potentially biologically significant, levels of in-plane LC stretch and compression (reaching 10%–25% medians and 20%–30% 75th percentiles). Deformations were sometimes highly focal and concentrated in regions as small as a few pores. Regions of largest displacement, stretch, compression, and shear did not colocalize. Displacements and strains were not normally distributed. Contralateral eyes did not always have more similar responses to IOP than unrelated eyes. Under elevated IOP, some LC regions were under bi-axial stretch, others under bi-axial compression.

Conclusions. We obtained eye-specific measurements of the complex effects of IOP on the LC with unprecedented resolution in uncut and unfixed human eyes. Our technique was robust to electronic and speckle noise. Elevated IOP produced substantial in-plane LC stretch and compression. Further research will explore the effects of IOP on the LC in a three-dimensional framework.

Keywords: lamina cribrosa, optic nerve head, biomechanics, glaucoma, strain, second harmonic imaging

Glaucoma is a leading cause of blindness worldwide.[1] Loss of vision in glaucoma is due to the degeneration of the retinal ganglion cell axons,[2] believed to initiate within the lamina cribrosa (LC).[3,4] Elevated IOP has been identified as a primary risk factor for the development and progression of glaucoma,[2,3] and lowering IOP remains the only proven treatment to reduce the risk of neural tissue injury.[5,6] Although much has been learned about the clinical risk factors,[2] the mechanisms by which neural tissue degenerates and the roles of IOP remain controversial.[2,7] The biomechanical paradigm of glaucoma postulates that an elevated IOP induces deformations of the LC, namely stretch, compression, and shear, which trigger a cascade of events that eventually lead to neural tissue damage.[7,8] Despite the importance of characterizing the effects of IOP on the lamina to understand glaucomatous neuropathy, it has not been possible to measure directly the effects of IOP on the LC with sufficient resolution to clarify the role of IOP on the laminar pores and trabeculae. Instead, research on the effects of IOP on the LC has relied on averaged[9–11] or indirect[12,13] measures, simulation,[14–16] or animal models.[11,17]

Our goal was to obtain high-resolution eye-specific measurements of the trabecular scale displacements and deformations induced in the human LC by an acute increase in IOP. We hypothesized that under these conditions, the tissues of the LC are subjected to substantial levels of stretch, compression, and shear, which could contribute to the biological vulnerability to elevated IOP. Further, we hypothesized that the differences in the effects of IOP between eyes of an individual are smaller than the differences between individuals.

Methods

General Strategy

Our general strategy was the following: the LCs of human donors were imaged using second harmonic-generated (SHG) imaging at various levels of IOP. An image registration technique was then used to find the transformation that brings an image acquired at low IOP into coincidence with one acquired at elevated IOP. From this transformation, we

computed the in-plane displacements and deformations produced by the increase in IOP, which we then analyzed to determine distribution and contralateral similarity.

Eye Preparation and Imaging

Six ostensibly healthy eyes from four human donors aged 23 to 82 years were scanned using SHG imaging. The details of the eye preparation and imaging have been described elsewhere.[18,19] Briefly, the eyes were obtained from the San Diego Eye Bank within 36 hours of death, and managed in accordance with the provisions of the Declaration of Helsinki for research involving human tissue. The eyes were cannulated with a 25-gauge sutureless trocar and cannula system attached to a reservoir of buffered saline solution. The protruding optic nerve was removed at the level of the sclera in a single pass by using a disposable cryostat blade, to allow imaging of the LC region without blockage from retrolaminar tissues. The entire eye was placed onto the microscope and held in place with moistened cotton gauze so that the posterior aspect of the optic nerve head (ONH) was oriented above the objective. Images up to a depth of 600 μm were acquired at IOPs ranging from 10 to 50 mm Hg (Zeiss 510 Meta LSM [Zeiss, Oberkochen, Germany] equipped with a titanium-sapphire femtosecond laser mode-locked at 820 nm, and backscattered SHG signals were collected using the Meta detector set to collect 400–420-nm emissions). Line averaging during acquisition was set between 2 and 4. At each pressure, the eyes were allowed to equilibrate for 30 minutes before imaging.[20] Mosaic lateral resolution varied from 1.76 to 4.97 μm/pixel. Resolution only varied between eye pairs, so that images from the same eye or contralateral eyes were always with the same resolution. We analyzed the effects of an IOP increase of 35 mm Hg (either 10–45 mm Hg or 15–50 mm Hg). The globes were allowed to rotate and translate during inflation so as not to introduce artifactual constraints. The image mosaics covered areas at least 20% wider than the scleral canal to avoid introducing artifacts during image registration, such as those that could arise due to changing field of view or moving boundaries. In this work we analyzed maximum intensity anterior-posterior projections of the LC.

Image Registration to Determine Displacements

To identify the transformation bringing the image acquired at low IOP into coincidence with the image acquired at elevated IOP, we used a multilevel finite element-based digital image correlation technique where the task of registration is formulated as a variational problem. This is a well-established and powerful technique within the general family of deformable registration algorithms.[21,22]

The algorithm is initialized by equalizing the histogram means and ranges of both images. An iterative process then proceeds in which the gradient of the similarity function is used to define external loads (forces) acting onto the finite element model (the meshed image), defining a system of equations that capture the image differences in a physical formulation, which is solved using finite element techniques (see Appendix). This produces a transformation (a displacement field) with which an updated provisional version of the transformed low IOP image is generated. The algorithm continues iteratively until the similarity function (potential energy) is minimized, indicating a maximal similarity between transformed low IOP and elevated IOP images, or an equilibrium is reached. Thus, in our formulation, the task of registering the images literally corresponds with a physical deformation of the LC, with the applied forces driving the registration being derived from the gradients in the similarity. An energy-based algorithm also meant that large deformations required proportionally larger differences between images.

Similarity between images was measured using normalized regional cross-correlation, in which the standard cross-correlation coefficient was extended to incorporate the neighborhood around a pixel. Thus, the measure takes into account the local image structure, which has the advantage that it does not assume that the intensity of a point in the tissue remains unchanged between images. The measure can account for linear intensity distortions in the image acquisition, noise, image angle, and other conditions that can produce changes between the images, and which are a consequence of unavoidable variations in illumination and reflectivity that naturally arise in SHG imaging.[18,19] These variations must be bridged to identify the optimal transformation without introducing spurious deformations that may improve image registration in an artifactual manner inconsistent with the tissue being a continuum. The continuity and smoothness requirements implicit into the deformations possible within a finite element formulation are therefore an important characteristic of our technique for describing the effects of IOP on the tissues of the ONH. A finite element–based algorithm using second-order elements with quadratic basis functions was found appropriate (results not shown). We used a multigrid approach in which the images are registered at multiple levels, with a solution first identified matching large-scale features with a coarse grid, and then passed on to finer grids, progressively matching smaller features and refining the agreement. An energy-based multigrid approach had several advantages. It increased efficiency, and allowed exploring the transformation space without the optimization process becoming trapped in a local minimum. Large deformations are possible, and local minima avoided, by splitting the deformation and applying the forces in small steps, and by using an iterative procedure in which linear models are used only to solve small deformations. The final total deformation is produced by concatenating the optimal small step deformations. In this study, we selected a linearly elastic, isotropic constitutive formulation for the tissues. We allowed for the tissue to be compressible to account for changes in projected area. We should note that this does not place undue constraints on the deformations, as large deformations can be accommodated through the local forces caused by the potential energy derived from the image similarity measure. Variations in material properties slightly altered the convergence path, but the same transformations were found. Appropriate parameters were identified in preliminary runs. The results presented were obtained using five grid levels with element sizes of 3 to 40 pixels and similarity neighborhood widths between 10 and 20 pixels.

Using the shape functions of the highest resolution finite element mesh, we computed the in-plane deformation matrix at each pixel, from which we computed the maximum (first) and minimum (second) principal strains.[23] The maximum in-plane shear strain was computed as the maximum difference between the principal strain magnitudes.[23]

Verification and Performance Evaluation

We set a series of test tasks to verify the image registration technique and evaluate its performance. First we used a set of synthetic deformations applied to an image acquired at low IOP (OD donor 2) to produce test-elevated IOP images. Our technique was then used to find the deformation by registering the original and test images, and its performance evaluated by comparing the known (imposed) displacement and deformation fields with those obtained using our technique. We considered the following synthetic deformations of progressively increasing difficulty:

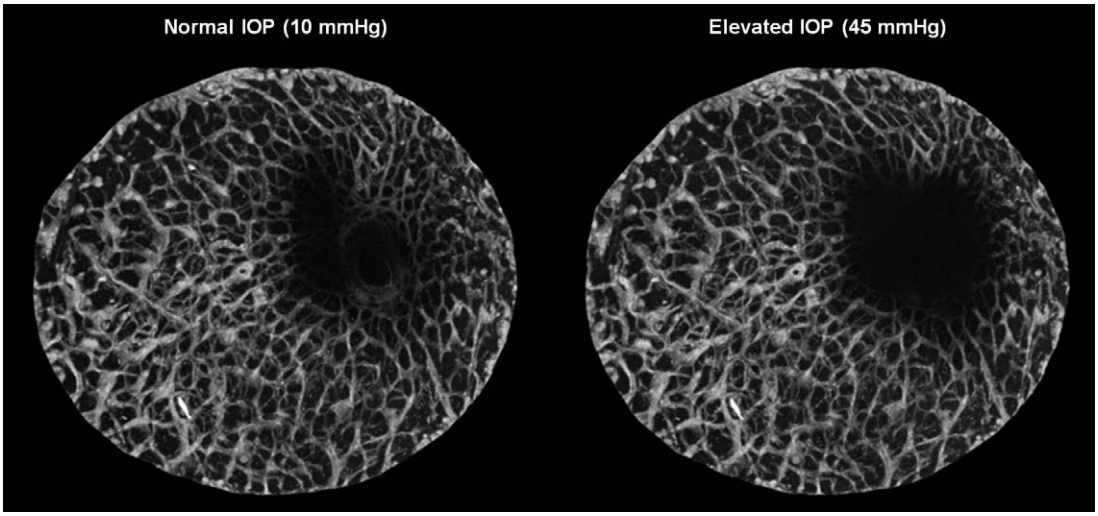

FIGURE 1. En-face SHG images of the LC of a 79-year-old eye (donor 2 OD) at normal (*left*) and elevated IOP (*right*). The borders of the scleral canal were segmented manually and the LC isolated for analysis. Note the rich horizontal (in-plane) trabecular structure characteristic of the laminar region visible without the need for labeling and with the neural tissues present.

1. rigid body translations of various magnitudes and directions;
2. linear tissue stretch (first principal strain of 5%);
3. radial stretch (first principal strain of 10%) from the geometric center of the LC; and
4. a deformation pattern obtained from our own technique matching low to elevated IOP images, intended to test our technique using a realistic complex deformation.

We further evaluated whether the algorithm had converged to a good solution using the following three tests:

1. Using landmarks manually placed on the low and elevated IOP images: A coauthor familiar with LC imaging, morphometry, and delineation (JLG) manually placed 35 landmarks in corresponding locations of both the low and elevated IOP images. Landmark placing on the elevated IOP image was repeated three times. Using the deformations obtained by our registration technique, the landmarks placed on the low IOP image were virtually deformed (transformed) to their corresponding locations at elevated IOP. We then evaluated the distance between the low IOP landmarks transformed to elevated IOP and the manually placed elevated IOP landmarks. This distance was then compared with the repeatability of identifying the landmark locations at elevated IOP. The distance between elevated IOP landmarks is a measure of landmark placement repeatability. A good transformation would result in transformed low IOP landmarks within the region defined by the elevated IOP landmarks.
2. Comparing pixel by pixel the differences in image intensity between the unregistered (initialized) and registered images.
3. Inspecting the images to use our experience to judge whether the technique had successfully registered the images. This qualitative approach, while not definitive, is important for verifying new algorithms.

Robustness to Image Noise

The magnitude and type of noise in our SHG images of the LC is unknown. To estimate these we measured the signal intensity in image regions with and without tissue (comparing two images of the same region at the same IOP registered manually). In both cases, the noises were well described by a normal distribution (Kolmogorov-Smirnov $P < 0.02$). Means (SD) were 0.7% (3.1%) and 1.6% (0.48%) of the image dynamic range for regions with and without tissue, respectively. Our goal was to evaluate the robustness of our image registration technique to noise. Specifically, we added various levels of noise to the images to be registered (donor 2 OD) and registered again. Two types of noise were considered: Gaussian and Exponential. Gaussian noise, also known as shot or electronic, is additive and can be well approximated by a Gaussian function. We added Gaussian noise with SDs of 4.0%, 8.0%, 12%, and 16%, and a mean of zero. Our algorithm normalizes by mean signal intensity, and is therefore insensitive to mean differences. Exponential noise, also known as speckle noise, is multiplicative with $I_{noise} = n\ I_{base}$, where n is randomly generated from a population that follows the negative exponential function $P(n) = (1/\beta)\ e^{-n/\beta}$.[79] We added Exponential noise with βs of 1 and 2. For each case with the added noise we compared the size of the differences in displacement magnitude with the baseline (no extra noise) as well as the distributions and contour maps of principal strains.

Analysis

For each eye, we analyzed the maps of displacements and deformations, as well as the distributions of each of these measures. Herein our focus was the effects of IOP on the LC, and therefore we excluded from analysis the central retinal vessels and tissues exterior to the scleral canal. We excluded regions of low contrast or low signal-to-noise ratio by manually identifying and marking them in each image. We also excluded from analysis any regions that showed any suspicious noise or variations in contrast or intensity that could indicate problems with the stitching. No filtering or averaging was applied. For visualization, but not for analysis, the images were processed to improve brightness and contrast using previously reported algorithms.[24] Image processing, visualization, and analysis were done using open source software (ITK,[25] Fiji,[26] Paraview,[27] and R[28]).

Investigative Ophthalmology & Visual Science

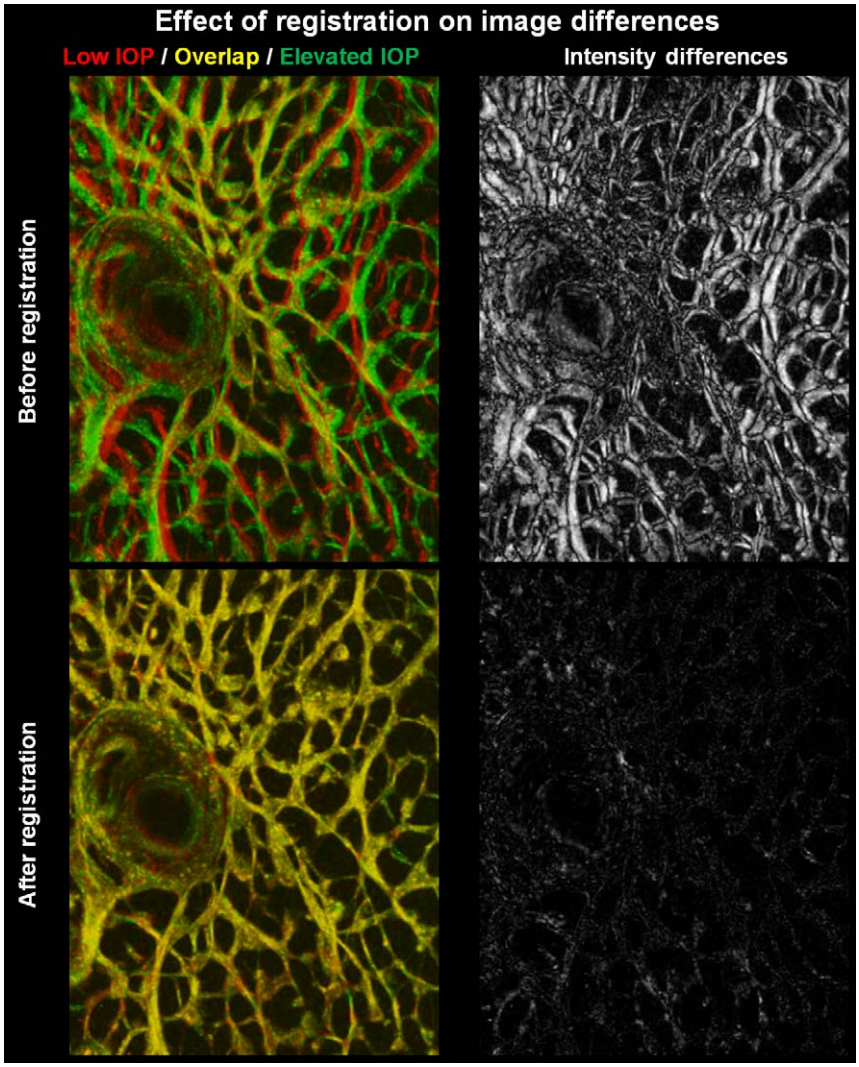

FIGURE 2. Demonstration of the image registration technique. Close ups of the LC of donor 1 before (*top*) and after (*bottom*) registration. The left side shows images acquired at low (*green*) and elevated IOP (*red*) to visualize the differences and overlap (*yellow*). The differences before registration cannot be removed by simple translation or rotation. The right side shows the differences in image intensity with the largest differences in white and smallest differences in black. The registration produced excellent coincidence between the images, without concentrations. The largest differences are due to noise and intensity variations that result in slightly greenish or reddish regions despite coincidence of LC features. Another useful visualization of the good results obtained from the registration is to use image flickering, as in the supplemental animation (Supplementary Movie S1) of a detail on the temporal side (*right side* of the image).

RESULTS

Images of the LC region at different IOPs were obtained (Fig. 1). The images show the pore and trabeculae structure traditionally defined as the LC,[9,11,17,29–33] with well-defined trabeculae and canal edges, with pixel intensities spread over the range of the imaging device (the dynamic range).

The image registration technique performed very well to match low and high IOP images (Figs. 2, 3). For the synthetic evaluation cases with no deformation, our technique found the known displacement precisely (to machine zero). This demonstrated that the meshing and boundary conditions do not preclude simple translations. In the rest of the synthetic cases, all results from our technique were very close to the known displacements and deformations, with differences in magnitude of displacement and deformations (for all strain measures) at every point always smaller than 1% (relative). In every case, the technique converged to the correct solution. Using manual landmark delineations, we found that the mean distance between the landmarks placed at low IOP transformed to the elevated IOP and the landmarks actually placed at elevated IOP were 3.4 pixels, which was smaller than the 4.2 pixels repeatability (mean distance between landmarks as placed in the elevated IOP images). The pixel-by-pixel comparison of image intensities established that the image differences remaining after the registration were much smaller than before registration, accounting for noise and illumination variability (Supplementary Fig. S1).

Applying the registration technique to the experimental data revealed that increases in IOP produced substantial in-plane tissue displacements and deformations (Fig. 4). LC close-ups illustrate various effects of IOP, and demonstrate the complexity of displacements and deformations produced by the increase in IOP. This complexity is also evidenced quantitatively in maps of IOP-induced tissue displacement, and deformation magnitude (Fig. 5). The regions of largest

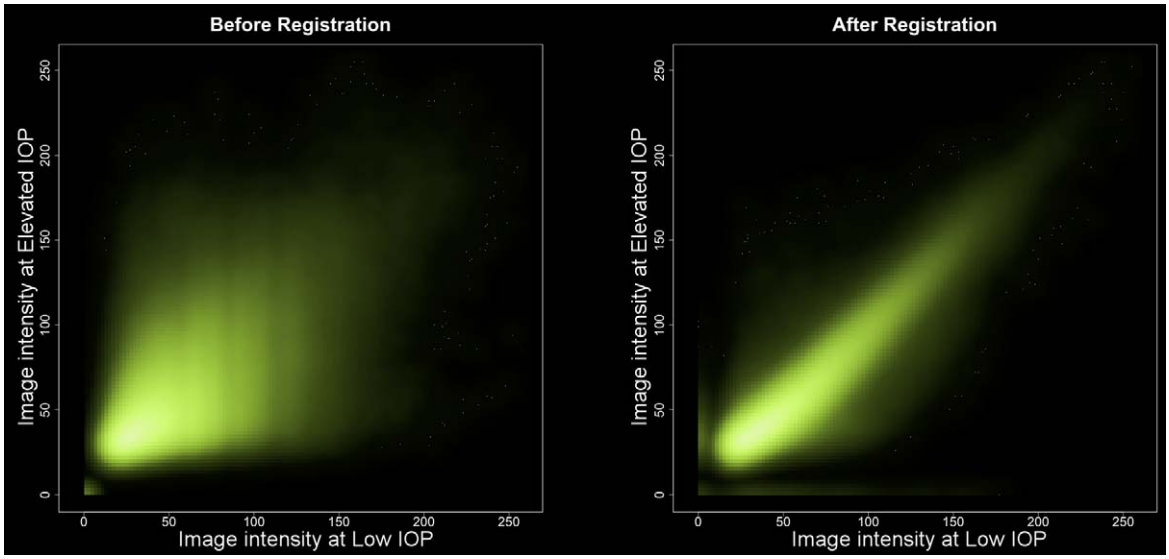

FIGURE 3. Effect of the registration technique on the distribution of differences in image intensity. We compared image intensities (pixel by pixel) between the SHG images acquired at low and elevated IOP before (*left*) and after (*right*) applying our image registration technique. Both comparisons above were done after registering the image centers of mass. The panels are density plots, akin to 2D histograms, where the brightness of a region is proportional to the number of cases. Notice the much wider cloud before registration, indicating large differences between images. Please see Supplementary Figure S1 for a binned Bland-Altman plot further illustrating the effects of registration.

displacements did not colocalize with the regions of largest deformation. Similarly, the regions of large stretch did not colocalize with large compression or large shear. Interestingly, the deformations were sometimes highly focal and concentrated in regions as small as a few pores (Fig. 6). Maps of image differences before and after registration demonstrate that this was not an artifact of the registration (Fig. 7).

Whereas both eyes of donor 3 had somewhat similar distributions of IOP-induced strain, the distributions for the eyes of donor 4 were quite different. One eye of donor 4 (OS)

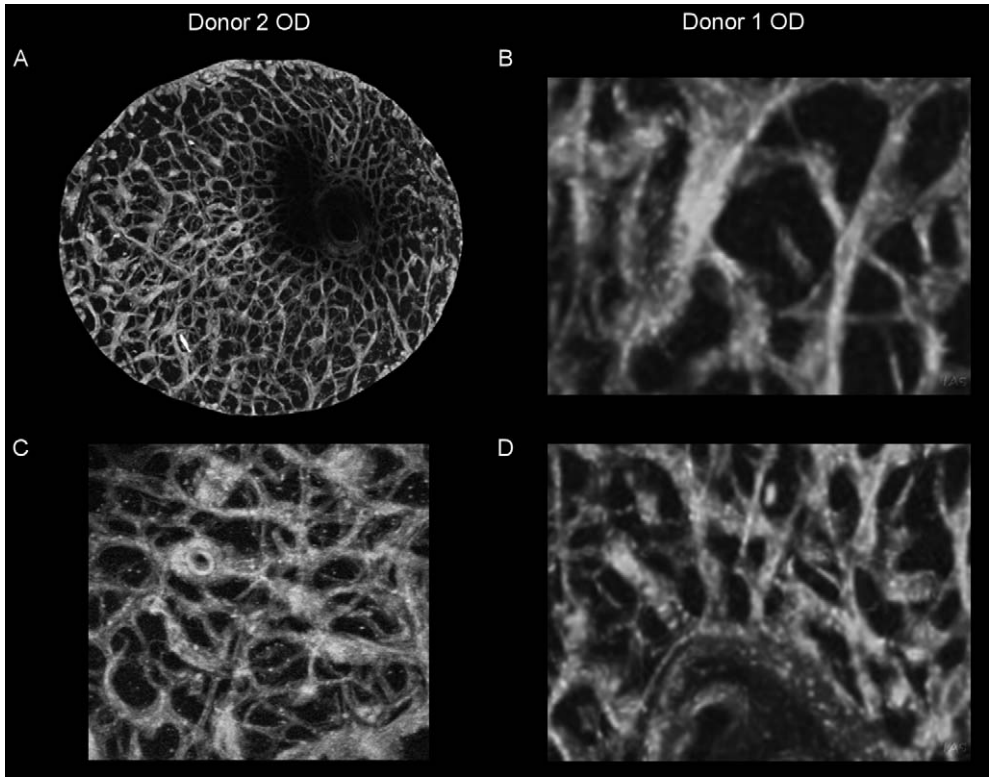

FIGURE 4. Applying the image registration technique. These animations show IOP-induced displacements and deformations produced by the increase in IOP from 10 to 45 mm Hg that are difficult to distinguish otherwise. Note the variations in beam thickness and pore sizes even within small regions. A small vessel can be distinguished in the LC close-up of donor 2 OD (**C**), which deforms differently from the surrounding tissues. The animations corresponding to (**A**), (**B**), (**C**), and (**D**) are 2, 3, 4, and 5, respectively.

Investigative Ophthalmology & Visual Science

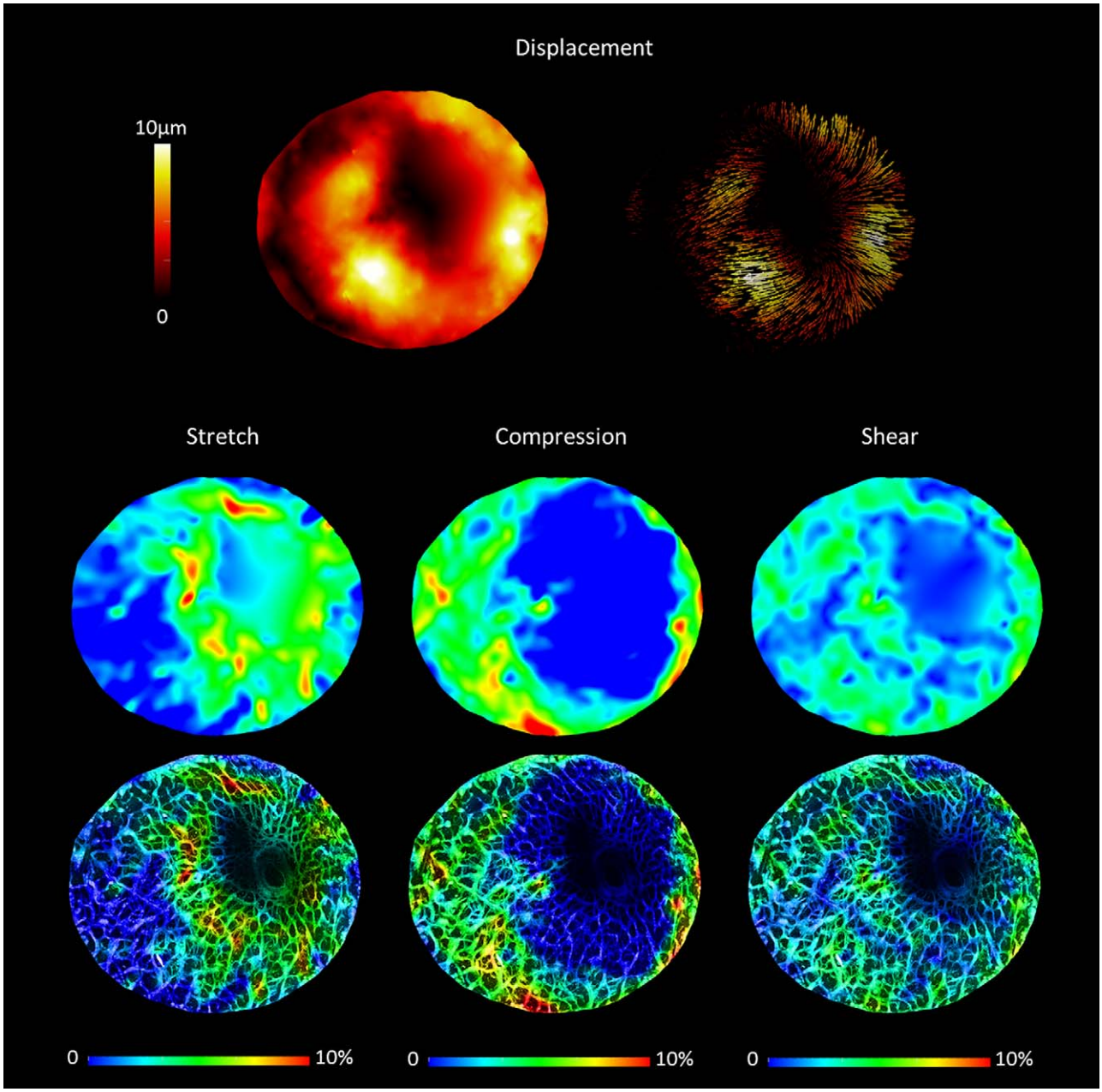

FIGURE 5. Effects of IOP. Displacement (*top row*) and deformations (*middle* and *bottom row*s) induced within the LC of donor 2 OD by an increase in IOP from 10 to 45 mm Hg. Shown are contour levels of displacement magnitude (*top left*) and displacement vectors on 5000 randomly selected points on the LC colored by the displacement magnitude (*top right*). The deformations are shown with contour-level plots of the magnitude of in-plane stretch (*left column*), compression (*middle column*), and shear (*right column*). To better appreciate the relationship between the deformations and the structures of the LC we show the contour levels of deformation (*middle row*) and the LC structure as imaged by SHG colored by the stretch, compression, and shear (*bottom row*). In-plane displacements are of the order of the anterior-posterior displacements measured by using OCT,[10] as predicted by modeling.[23,43] Displacements, and compressive and shear deformations were smaller near the main vessels. The regions of largest displacement, stretch, compression, and shear did not colocalize. Shear strains in this eye did not have as high peaks as the stretch or compression.

had distributions similar to those of the eyes of donor 3, whereas the other eye (OD) had distributions similar to the OD of donor 2. Some, but not all, of the IOP-induced displacements and deformations were normally distributed (Fig. 8). The distributions are summarized using box plots (Supplementary Fig. S2). The sensitivity analysis demonstrated that the registration technique was highly robust to image noise (Fig. 9).

The tissues suffer the various deformations simultaneously, and therefore it is useful to visualize the effects of IOP using density plots (Fig. 10). The plots are akin to bidimensional histograms, showing darker clouds in the regions with more measurements. The clouds span three quadrants, indicating a rich response to IOP, with multiple modes of deformation. Again, increases in IOP had similar effects on the eyes of donor 3 but rather different on the eyes of donor 4, who suffered much smaller strains for the same increase in IOP. To illustrate

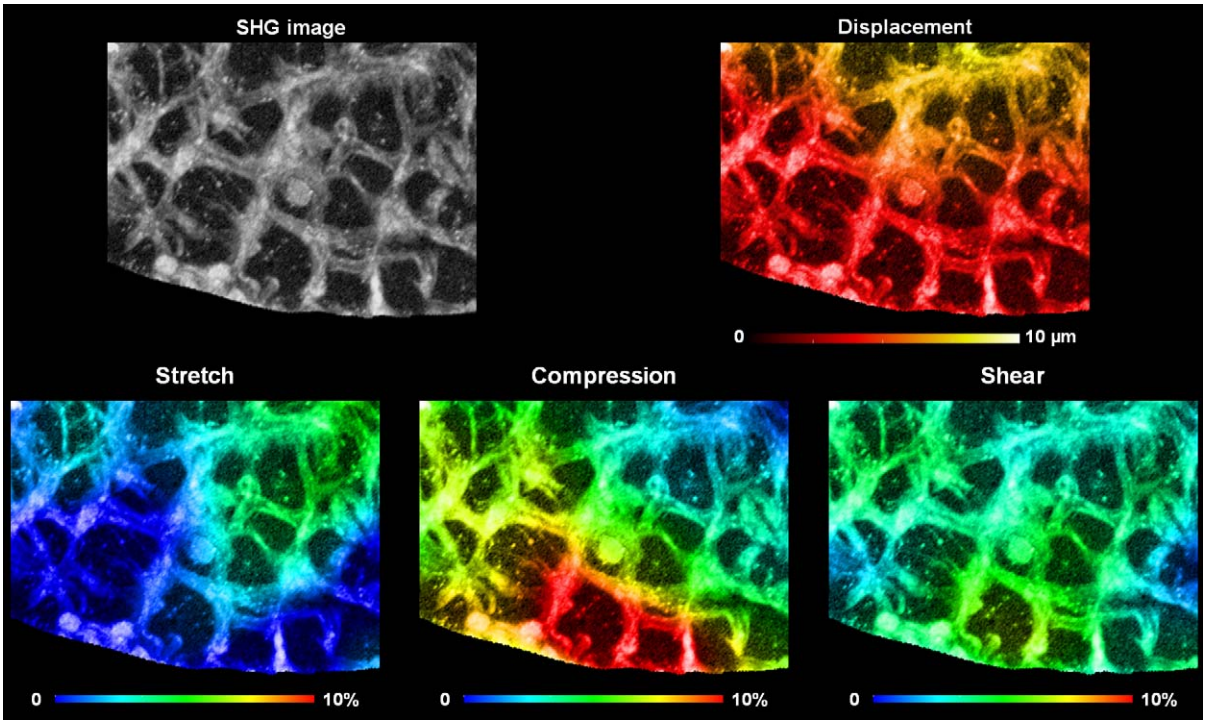

FIGURE 6. Detail of the biomechanical effects of IOP. To better appreciate the local nature of the effects of IOP we show in this figure a detail of the peripheral region of donor 2 OD. The panels show the structure of the LC in the SHG image (*top left*), as well as the SHG image colored by the magnitudes of displacement (*top right*), stretch (*bottom left*), compression (*bottom center*), or shear (*bottom right*). Notice the concentration of compressive strains in two pores that appear otherwise unremarkable. These pores are not highlighted by either the displacements or other modes of deformation.

how the deformation mode varies over the tissues of the LC, we color-coded three modes of deformations (Fig. 11), each one a quadrant in Figure 10. In this eye, the region near the central vessels was under biaxial stretch and regions in the periphery under biaxial compression.

DISCUSSION

We present high-resolution (trabecula-scale) eye-specific measurements of the displacements and deformations induced within the LC by an acute increase in IOP. Three main results arise from this work: first, increases from physiologic to elevated IOP produced substantial, and potentially biologically significant, levels of in-plane LC stretch and compression; second, the regions of largest IOP-induced displacement, stretch, compression, and shear did not colocalize; and third, contralateral eyes did not always have more similar responses to IOP than unrelated eyes. Below we consider each of these in turn.

Main Results

Increases From Physiologic to Elevated IOP Produced Substantial, and Potentially Biologically Significant, Levels of In-Plane LC Stretch and Compression. Although much has been learned about the effects of IOP on the tissues of the ONH, the mechanisms by which the IOP-induced forces and deformations contribute to neural tissue degeneration and loss of vision are still not well understood.[8] These mechanisms have been proposed to involve stretch, shearing, or kinking of the retinal ganglion cell axons,[8,34,35] disruption of axoplasmic flow,[3,36,37] compromised perfusion,[38,39] and others.[4,34,36,40–42] A better characterization of the effects of IOP on the LC using methods such as those presented herein will contribute to evaluation of these hypotheses. Most studies of ONH biomechanics have focused on the IOP-induced anterior-posterior displacements of the LC. We have shown here that the in-plane (lateral) displacements of the LC are also prominent, reaching levels comparable to those that have been shown to be of biological significance to LC astrocytes.[23,43] Experiments have established that both tissues[44] and individual cells[35,45–47] are sensitive to mechanical stimuli, and that their sensitivity varies depending on the mode, magnitude, and temporal profile of the stimulus. Sensitivity includes upregulation and downregulation of hundreds of genes.[35,36,45,46] We have shown that the highly focal effects of IOP observed were not an artifact of the image registration technique.

The complex biomechanical environment within the ONH had been predicted by us[14,48,49] and others,[12,15,16,50–56] and was, therefore, not a surprising finding. It was surprising, however, to find that the shearing strains were sometimes substantially smaller than the tensile or compressive strains. We should point out that direct comparison of strain magnitudes may not be appropriate to determine their relative effects, as tissues may be more sensitive to shear than to stretch or compression.[57] Studies of neural tissue damage in the brain and spine have found these tissues particularly sensitive to shearing strains.[57,58] The potential biological significance of the biomechanical effects of IOP on the tissues of the LC is discussed in more detail elsewhere.[8,34,35] Note that in this work we have studied the in-plane deformations, and the three-dimensional (3D) tissue deformations could be different.

The Regions of Largest IOP-Induced Displacement, Stretch, Compression, and Shear Did Not Colocalize. Each effect of IOP had a different distribution over the LC, with

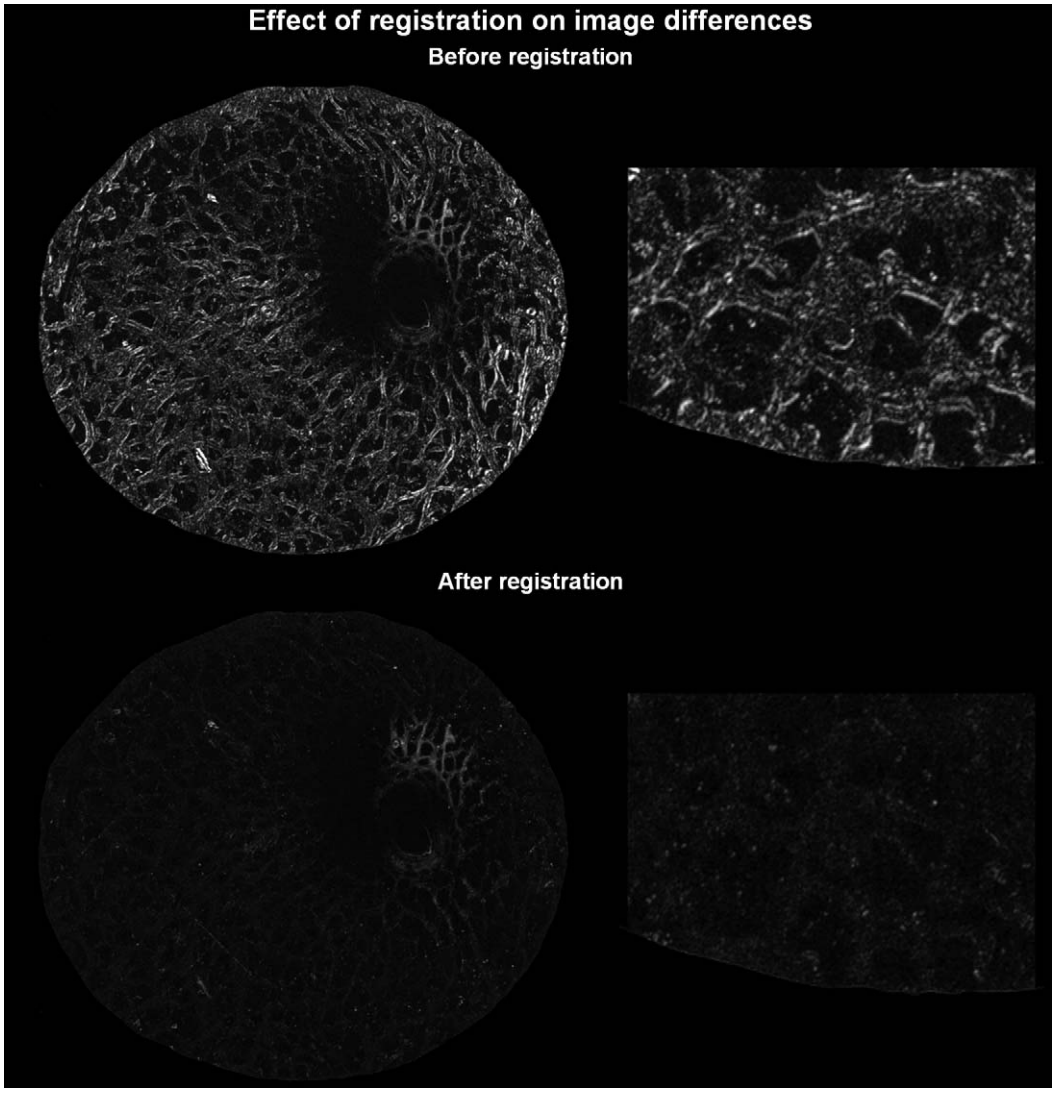

FIGURE 7. Image differences before and after registration. Pixel-by-pixel comparisons of differences in intensity between the images acquired at low and elevated IOP before (*top*) and after (*bottom*) image registration (donor 2, OD). Shown are whole LCs (*left*) and details (*right*) of the peripheral region in Figure 6. Largest differences are shown in white and smallest differences in black. Note the uniform distribution of differences after registration, demonstrating that the local effects shown in Figure 6 are not an artifact of the registration.

the maximum stretch being the most similar to the displacement magnitude, and the maximum compression the least. Although this seems natural from a theoretical perspective (i.e., there is no reason a priori for the large derivatives of displacement to colocalize with the large values for the displacement), it has been speculated that larger displacements implied larger deformations.[9,10,12]

Some LC regions were subjected to bi-axial compression. This is interesting because it raises questions on the role of the load-bearing connective tissue fibers within these regions. Collagen-based materials are traditionally conceived as highly efficient in carrying tensile loads, and poor for supporting compression or bending.[51] Studies of collagen fibers have shown that lack of tensile loads result in a substantial increase in sensitivity to collagen-digesting enzymes.[59] We did not measure the full 3D deformation, and it is possible that the 3D deformation was not only compressive. Nevertheless, the question stands for the horizontal LC trabeculae. We suspect that analysis of other loading conditions, such as intermediate levels of IOP or fluctuations in cerebrospinal fluid pressure,[29,31,60–62] will show that these trabeculae are sometimes subjected to in-plane stretch.

Contralateral Eyes Did Not Always Have More Similar Responses to IOP Than Unrelated Eyes. Some eye pairs had similar responses to IOP, whereas others had notably different ones. Thus, it cannot be concluded that the differences in the effects of IOP between eyes of an individual are always smaller than the differences between individuals.

Our results should be interpreted weighing carefully the virtues and limitations of our methods. We have discussed elsewhere those related to SHG imaging of the LC.[18,19] Below we summarize earlier discussions, with a focus on the virtues and limitations most relevant to this work. We begin with the virtues: The measurements presented here were obtained from human eyes, and can therefore be more directly related to patients than those obtained from nonhumans, which are commonly used for research on ONH biomechanics. We have presented eye-specific measurements that did not require

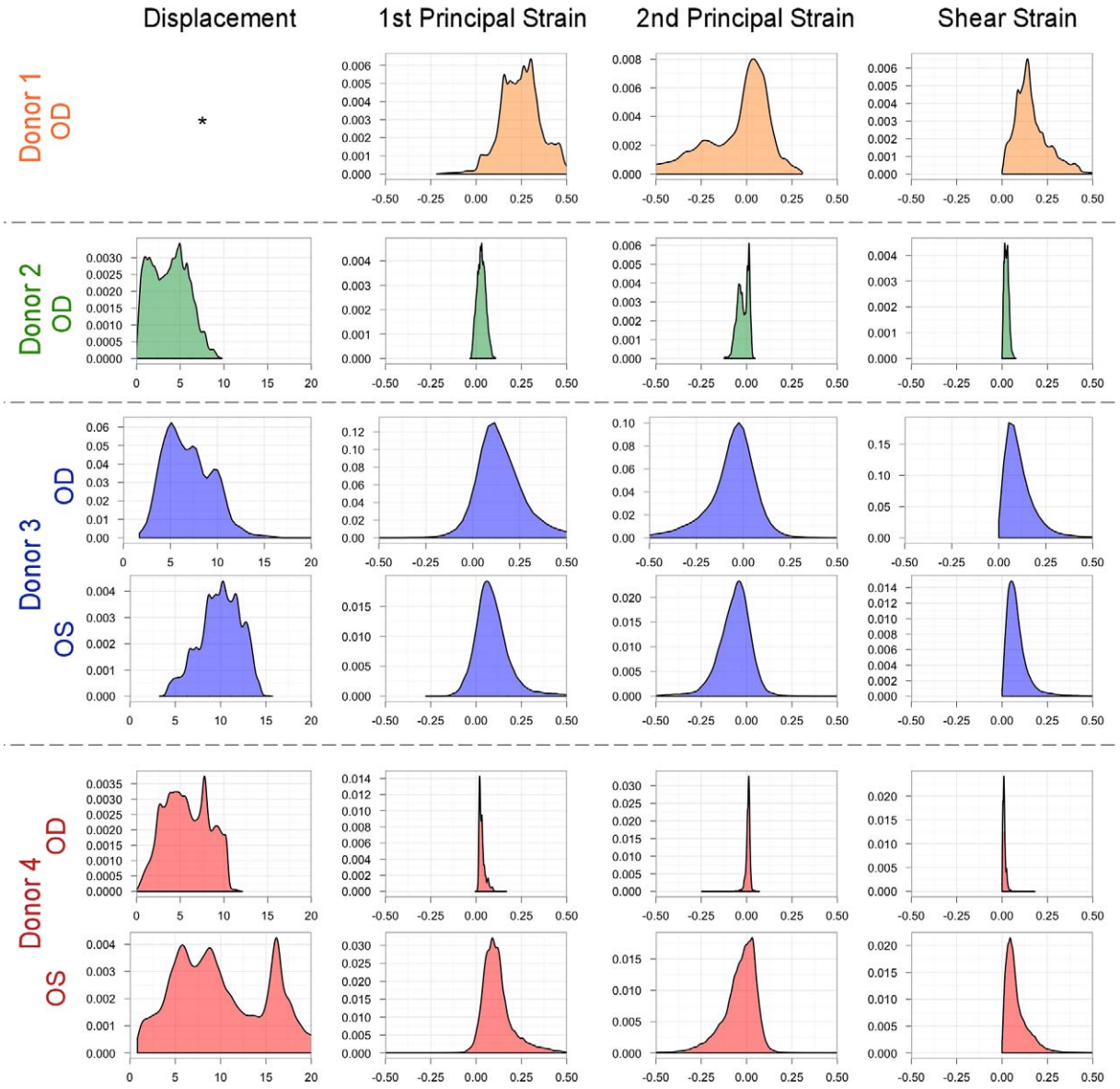

FIGURE 8. Distributions of displacements and deformations for the LCs of six eyes. Positive strains represent tissue stretch, whereas negative strains represent tissue compression. Shown is the absolute value of the shear strain. Clearly the increases in IOP produced substantial displacements and levels of strain that have been demonstrated to be of biological significance.[35,45,46] Notice that the effects of IOP were similar between the eyes of donor 3, but notably different between the eyes of donor 4. The scale of the images acquired from the LC of donor 1 could not be ascertained reliably, and therefore we excluded the displacements computed from it from analysis. Recall that zero strain corresponds with no IOP-induced deformation, while still allowing for local translation.

assumptions on contralateral similarity[9,33,63] or population generalizations.[15,29,48,64] Our results suggest that the assumption of contralateral similarity may not always apply to human eyes. The resolution and level of detail with which we have been able to measure the in-plane IOP-induced displacements and deformations of the tissues of the LC are unprecedented. Our results do not depend on assumptions on boundary conditions or tissue constitutive properties or symmetry that are necessary for numerical or analytical biomechanical models.[14,51–53] We measured the effects of IOP on the internal tissues of the ONH, not on the surface, which have been shown to be poor surrogates for the interior.[10,43,63] The tissues were not fixed, labeled, or sectioned. Thus, the results are not affected by artifacts that arise during tissue processing, such as shrinkage, warping, or uneven labeling.[8,65] Our images were not subject to shadows from vessels, pigment, or the sclera that affect other imaging techniques, such as optical coherence tomography (OCT), and that occlude large regions of the LC.[33,66–69] Our technique was robust to image noise, both electronic and speckle, as we obtained effectively identical results even for noise levels substantially larger than expected on SHG images of the LC. We measured various modes of in-plane deformation that have been proposed to be critical contributors to tissue sensitivity to IOP, but that are not well understood and remain to be characterized.[8,35,57]

Limitations

The study was conducted on postmortem tissues, and we cannot exclude the possibility of some necrotic changes. The properties of the sclera, in particular, are important because they are a major determinant of ONH biomechanics.[56,62,70,71]

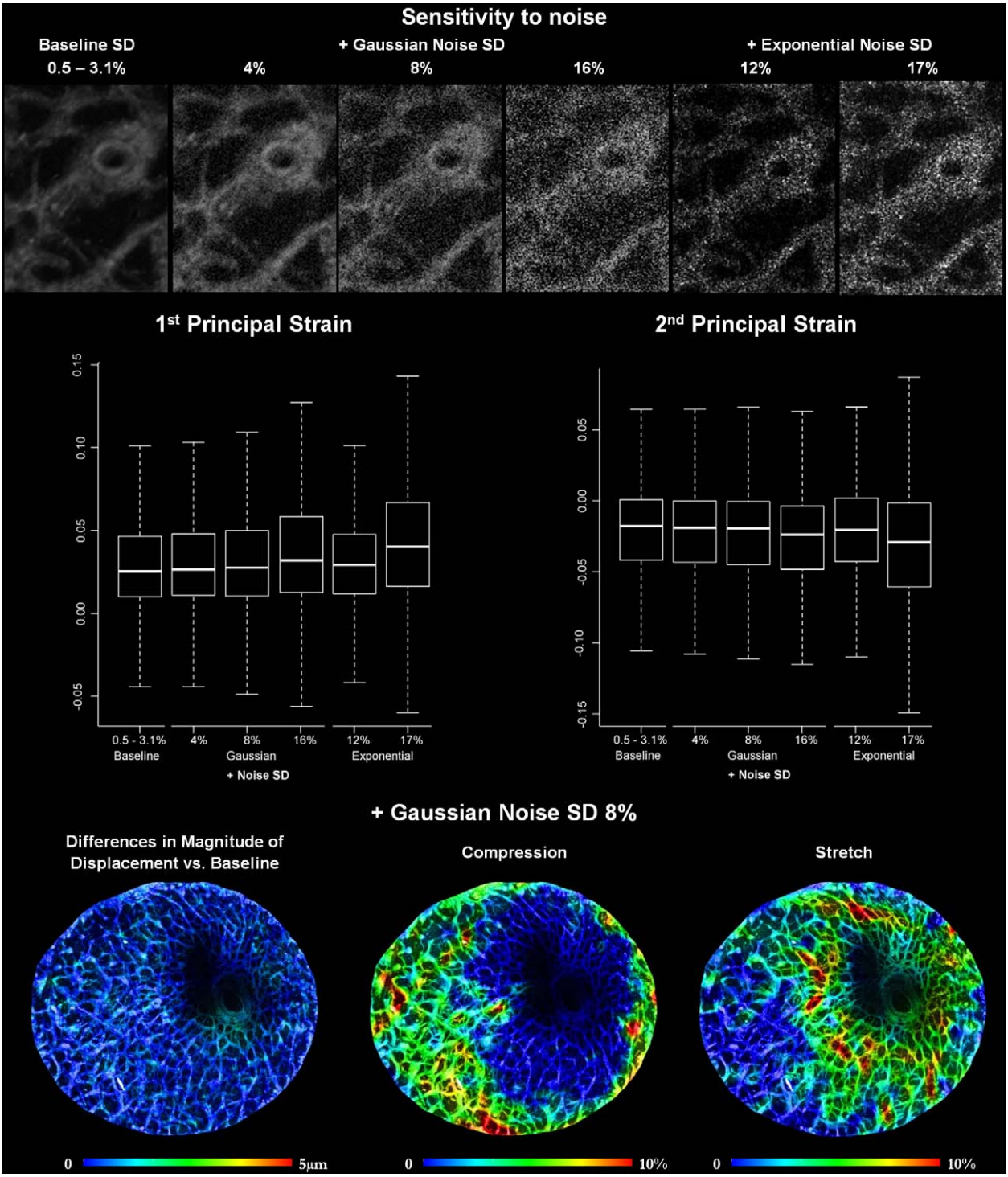

FIGURE 9. Sensitivity to noise. The robustness to image noise was evaluated by adding various levels of noise to the images before registration. Electronic noise was approximated by a Gaussian distribution with mean zero and SD of 4%, 8%, 12% (not shown), and 16%. Speckle noise was approximated as described in the text using a negative exponential function producing noise with SD of 12% and 17%. Data in this figure are for the LC of donor 2 OD. The *top row* shows details of the LC of donor 2 baseline image (*left*) and with added noise. The *middle row* shows box plots of the distributions of first and second principal strains (magnitudes). Adding noise had only small effects on the quartiles of the principal strain, although a few differences were noted on the extremes (5th and 95th percentiles). The *bottom row* shows contour level plots of the differences in magnitude of displacement (absolute values, *left side*), compression (*middle*), and stretch (*right*). Comparing the plots with those in Figure 5 shows that the displacements and deformations were highly robust to noise. As in Figures 5 and 6, the brightness of the contour levels of displacement and deformation is mapped to the intensity of the SHG images, simplifying seeing the tissue structure.

Investigative Ophthalmology & Visual Science

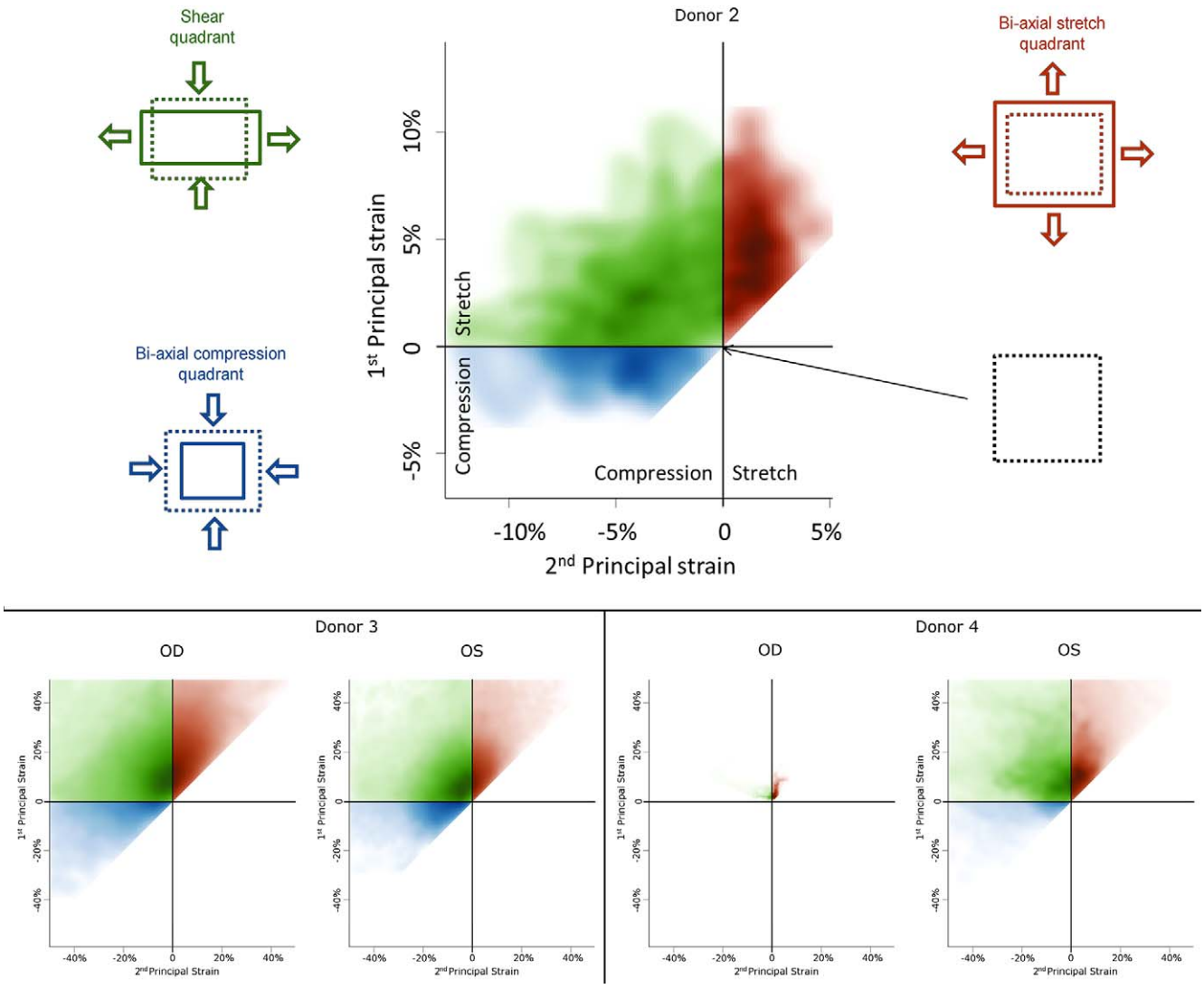

Figure 10. Two-dimensional distributions of principal strains illustrating modes of deformation and contralateral eye similarity/differences. The panels show density plots, with darker regions representing larger LC areas with the corresponding magnitudes of first and second principal strains. By definition, the principal strains are orthogonal and the first principal strain is greater than the second principal strain. Hence there are no measurements below the identity line. Positive strains correspond to tissue stretch and negative strains to tissue compression. Note that our analyses did not enforce conservation of volume. When both principal strains are positive (*top right quadrant*), the tissue is stretched in all directions (bi-axial stretch). When both principal strains are negative (*bottom left quadrant*), the tissue is compressed in all directions (bi-axial compression). When one principal strain is positive and the other negative (*top left quadrant*), the tissue is stretched in one direction and compressed in the other, in a state of shear. The special cases when both principal strains are equal correspond to equi-bi-axial stretch, equi-bi-axial compression, or the trivial case with no deformation (the origin). Recall that zero deformation does not have to imply zero displacement. Note the high magnitude of the deformations in most eyes, with strains in some small regions reaching into the 30% and 40%, consistent with the plots of Figure 8. Donor 4 OD suffered no bi-axial compressive strains, and was therefore in tension or shear. Thus, the effects of IOP on donor 4 OD were substantially different from those on donor 4 OS, and did not just differ on magnitude.

Experiments have suggested that the mechanical properties of the sclera do not change up to 72 hours postmortem.[72] Similarly, the experiments were carried out without a pressurized vascular system, which could have affected the mechanical behavior of the LC.[57] We cannot dismiss the possibility that sectioning the optic nerve to gain access to the LC may have altered LC biomechanics. The results obtained were derived from a two-dimensional (2D) analysis on projected images. Although we were careful to image the LC always in the same direction, some of the more complex effects of the 3D deformations would not be inferred by our analysis and may even result in inaccurate measurements. However, the focal nature of the deformations is inconsistent with whole ONH tilting or rotation. In-plane stretch, compression, or shearing of the retinal ganglion cell axons or of the capillaries supporting the tissues within the canal in the magnitudes we report may be sufficient insult to trigger a detrimental cascade of events. The data acquired through the SHG imaging is 3D, and our technique can be extended to 3D. Hence, analysis in 3D is possible, and is a logical next step. Historically, critical insight on the LC and ONH has been gained from studies using 2D imaging or analysis.[2,9,11,29,30,34,36,65,73,74] We imaged the tissues from the posterior direction, which means that the tissues observed may be different from what is typically observed using OCT, or identified in labeled histology. The horizontal trabecula-like structure makes us confident that we have imaged the LC region, even if incomplete. Laser penetration may have been reduced by effects of the

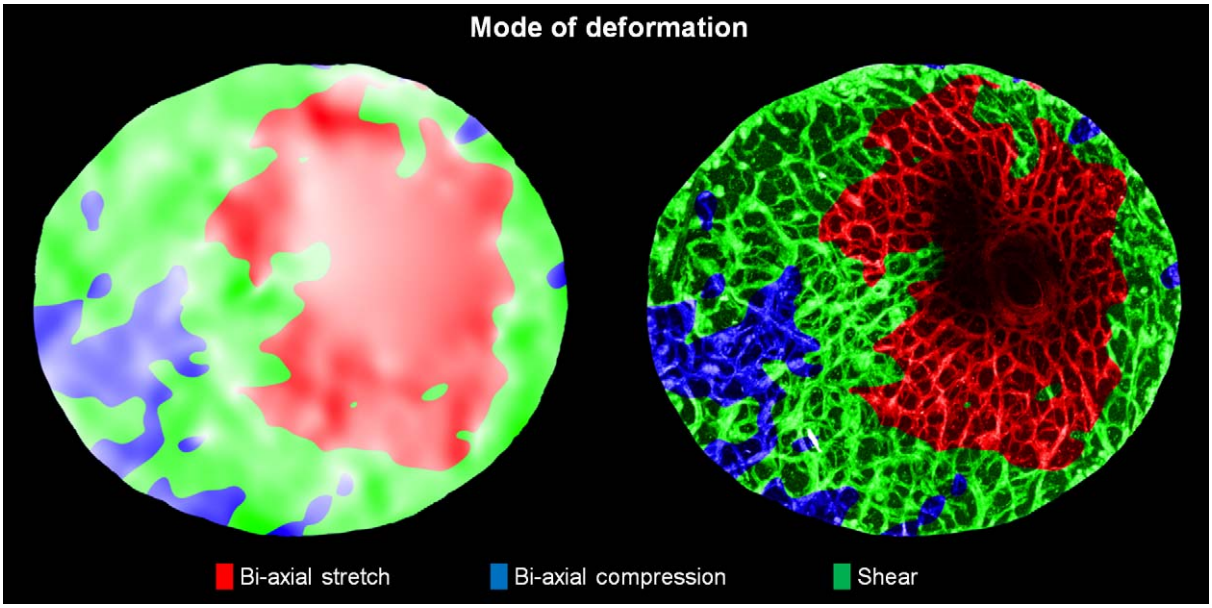

FIGURE 11. Spatial distribution of the modes of deformation of the LC of donor 2. Illustration of the spatial distribution of the three modes of deformation described in Figure 6. The colors represent whether locally the tissue is under bi-axial stretch (*red*), bi-axial compression (*blue*), or shear (*green*). In the plot on the *left*, the color intensity corresponds to the magnitude of the effect (distance from the origin in Figure 10), such that *white* represents zero deformation. In the plot on the *right* we used only *red*, *green*, and *blue* to color the SHG image to illustrate the spatial distribution of the modes, and overlaid the colors on the SHG image to show how the modes of deformation correspond with the LC structure. Note how the region near the vessels is in bi-axial stretch and most of the bi-axial compression occurs in the peripheral LC, often concentrated on specific pores.

retrolaminar septa.[75] Although our goal was to image the whole LC, imaging the posterior LC is important because experiments[76,77] and modeling[15,52,78] suggest that the posterior LC is an active region, critical for the sensitivity to IOP, remodeling, aging, and progression of glaucoma. For clarity and conciseness, in this work we analyzed the effects of IOP on the LC, although the tissues surrounding the LC, and in particular the sclera, are also critical to LC biomechanics and overall sensitivity to IOP.[14,17,49] In future work we will extend our analysis to neighboring tissues. In this study, we considered only differences between a physiologic and a substantially elevated IOP. Our intention was to find bounds for the displacements and deformations under the assumption that large, but still realistic, increases in IOP would be more likely to result in meaningful insight into the biomechanical effects on the ONH. During the experiments, images were acquired at several intermediate IOP levels. Analysis of these data will allow determining in more detail the complex nonlinear effects of IOP on the ONH. Although we acknowledge that the sample size was small, we point out that the results are consistent across eyes and therefore we believe valuable to the ocular biomechanics community. Because of the sample size, we emphasize direct comparison of the measurements over statistical tests. It is important to point out that the animations (Supplementary Movies S2–5) were generated by interpolating between the low and elevated IOP levels. The animations are intended to help distinguish effects of IOP that are difficult to visualize otherwise, such as small deformations or regional differences in response. The paths followed by the structures in intermediate IOP levels may differ. We also acquired images at the intermediate levels, and are currently in the process of analyzing them.

In the process of obtaining the results shown and discussed above, we introduced a technique for image registration that also merits discussion. We verified the technique and evaluated its performance through several tests. In all the tests, the technique was shown as accurate and appropriate for the task. Use of synthetic deformations is a standard technique for verification and has been applied in ocular biomechanics.[79] The evaluations using differences in image intensity and visual examination demonstrated excellent correspondence between the images after registration, supporting our confidence in the results. Although our test using manually placed landmarks also supports the results, it is our impression that this was helped by a relatively low repeatability in the placement of landmarks in the images at elevated IOP. Repeatable manual placement of landmarks in a complex 3D structure is not a simple task.[32,80] The challenge of achieving high repeatability in manual landmark placement emphasizes the need for an automated technique for image registration resilient to image variations. Our goal was the development of a robust technique that could be relied on to identify the transformation between the low and elevated IOP images. Hence, we opted for a registration and search strategy that would be resistant to artifacts from noise or uneven illumination. Computational efficiency was secondary to accuracy for the problem at hand, and it is possible that we will have to implement more advanced search strategies, such as genetic algorithms, when applying our technique to 3D analysis. Further improvements for speed may come from more efficient meshing strategies, such as an adaptive meshing approach in which smaller elements are used in structures requiring a fine mesh and larger elements in regions where the structure and deformations so require. It may also be beneficial to tailor the mesh by assigning different mechanical properties to the various tissues, or perhaps assigning properties from experiments. It also may be helpful to weigh the similarity measure to more strongly drive the convergence in the regions of interest. The trabecular nature of the LC provided an excellent structure for registration, rich in natural landmarks (information) for registration of LC trabeculae. Registration within the pores, where the SHG signal was lowest, was difficult, as the

information content and signal to noise were lower than in the beams. Thus, measurements of deformation within the pores should be taken to represent averages from the well-constrained deformations in the neighboring trabeculae. Nevertheless, we should point out that our technique used for registration all the pixels in the LC region of the images. Our technique is not restricted to registering the images at a set of landmarks, or the nodes of a mesh, which may optimize registration at those points, often compromising the registration elsewhere.[81] Note that the use of a finite element-based technique, with associated mechanical properties and forces producing image deformation, does not mean that we have modeled mechanically the effects of IOP on the tissues. Our method should not be construed as a type of inverse modeling, as the forces deforming the tissues are derived from the similarity neighborhoods and not IOP.

In summary, we presented eye-specific measurements of IOP-induced displacements and deformations of unprecedented resolution obtained from uncut and unfixed human eyes. This is an important step toward understanding the mechano-biological effects of IOP on the tissues of the optic nerve head, and their role in glaucomatous optic neuropathy. We have demonstrated that our technique is robust to electronic and speckle noise. Further work is needed to determine the biological effects of LC tissue stretch and compression of the magnitudes we measured, and if contralateral similarity in sensitivity to IOP is the rule or the exception in humans.

Acknowledgments

We thank Kitware (Clifton Park, NY), the developer of ITK, VTK, and Paraview for making these packages and their source code available.

Supported in part by National Institutes of Health (Bethesda, Maryland) Grants P30-EY008098 and EY019719; Eye and Ear Foundation (Pittsburgh, Pennsylvania); and unrestricted grants from Research to Prevent Blindness (New York, New York).

Disclosure: **I.A. Sigal**, None; **J.L. Grimm**, None; **N.-J. Jan**, None; **K. Reid**, None; **D.S. Minckler**, None; **D.J. Brown**, None

References

1. Resnikoff S, Pascolini D, Etya'ale D, et al. Global data on visual impairment in the year 2002. *Bull World Health Organ*. 2004; 82:844–851.
2. Quigley HA. Glaucoma: macrocosm to microcosm the Friedenwald lecture. *Invest Ophthalmol Vis Sci*. 2005;46: 2662–2670.
3. Minckler DS, Bunt AH, Johanson GW. Orthograde and retrograde axoplasmic transport during acute ocular hypertension in the monkey. *Invest Ophthalmol Vis Sci*. 1977;16: 426–441.
4. Quigley HA. Neuronal death in glaucoma. *Prog Retin Eye Res*. 1999;18:39–57.
5. AGIS Investigators. The Advanced Glaucoma Intervention Study (AGIS): 7. The relationship between control of intraocular pressure and visual field deterioration. The AGIS Investigators. *Am J Ophthalmol*. 2000;130:429.
6. Gordon MO, Beiser JA, Brandt JD, et al. The Ocular Hypertension Treatment Study: baseline factors that predict the onset of primary open-angle glaucoma. *Arch Ophthalmol*. 2002;120:714–720; discussion 829–730.
7. Burgoyne CF. A biomechanical paradigm for axonal insult within the optic nerve head in aging and glaucoma. *Exp Eye Res*. 2011;93:120–132.
8. Sigal IA, Ethier CR. Biomechanics of the optic nerve head. *Exp Eye Res*. 2009;88:799–807.
9. Yan DB, Coloma FM, Metheetrairut A, Trope GE, Heathcote JG, Ethier CR. Deformation of the lamina cribrosa by elevated intraocular pressure. *Br J Ophthalmol*. 1994;78:643–648.
10. Agoumi Y, Sharpe GP, Hutchison DM, Nicolela MT, Artes PH, Chauhan BC. Laminar and prelaminar tissue displacement during intraocular pressure elevation in glaucoma patients and healthy controls. *Ophthalmology*. 2011;118:52–59.
11. Fatehee N, Yu PK, Morgan WH, Cringle SJ, Yu DY. Correlating morphometric parameters of the porcine optic nerve head in spectral domain optical coherence tomography with histological sections. *Br J Ophthalmol*. 2011;95:585–589.
12. Albon J, Purslow PP, Karwatowski WS, Easty DL. Age-related compliance of the lamina cribrosa in human eyes. *Br J Ophthalmol*. 2000;84:318–323.
13. Morgan WH, Yu DY, Cooper RL, Alder VA, Cringle SJ, Constable IJ. The influence of cerebrospinal fluid pressure on the lamina cribrosa tissue pressure gradient. *Invest Ophthalmol Vis Sci*. 1995;36:1163–1172.
14. Sigal IA, Yang H, Roberts MD, et al. IOP-induced lamina cribrosa deformation and scleral canal expansion: independent or related? *Invest Ophthalmol Vis Sci*. 2011;52:9023–9032.
15. Roberts MD, Sigal IA, Liang Y, Burgoyne CF, Downs JC. Changes in the biomechanical response of the optic nerve head in early experimental glaucoma. *Invest Ophthalmol Vis Sci*. 2010;51:5675–5684.
16. Bellezza AJ, Hart RT, Burgoyne CF. The optic nerve head as a biomechanical structure: initial finite element modeling. *Invest Ophthalmol Vis Sci*. 2000;41:2991–3000.
17. Bellezza AJ, Rintalan CJ, Thompson HW, Downs JC, Hart RT, Burgoyne CF. Deformation of the lamina cribrosa and anterior scleral canal wall in early experimental glaucoma. *Invest Ophthalmol Vis Sci*. 2003;44:623–637.
18. Brown DJ, Morishige N, Neekhra A, Minckler DS, Jester JV. Application of second harmonic imaging microscopy to assess structural changes in optic nerve head structure ex vivo. *J Biomed Opt*. 2007;12:24–29.
19. Winkler M, Jester B, Nien-Shy C, et al. High resolution three-dimensional reconstruction of the collagenous matrix of the human optic nerve head. *Brain Res Bull*. 2010;81:339–348.
20. Sigal IA, Flanagan JG, Tertinegg I, Ethier CR. Reconstruction of human optic nerve heads for finite element modeling. *Technol Health Care*. 2005;13:313–329.
21. Hamarneh GA, Chu VA, NBordalo-Rodrigues MB, Schweitzer MC. Deformation analysis of Hoffa's fat pad from CT images of knee flexion and extension. In: Amini AA, Manduca A, eds. *SPIE Proceedings Medical Imaging 2005: Physiology, Function, and Structure from Medical Images*. Bellingham, WA: SPIE, 2005:527–534.
22. Sundaram TA, Gee JC. Towards a model of lung biomechanics: pulmonary kinematics via registration of serial lung images. *Med Image Anal*. 2005;9:524–537.
23. Sigal IA, Flanagan JG, Tertinegg I, Ethier CR. Predicted extension, compression and shearing of optic nerve head tissues. *Exp Eye Res*. 2007;85:312–322.
24. Kagemann L, Wollstein G, Ishikawa H, et al. Visualization of the conventional outflow pathway in the living human eye. *Ophthalmology*. 2012;119:1563–1568.
25. Ibanez L, Schroeder W, Ng L, Cates J. *The ITK Software Guide. 2nd ed*. Clifton Park, NY: Kitware Inc.; 2005.
26. Schindelin J, Arganda-Carreras I, Frise E, et al. Fiji: an open-source platform for biological-image analysis. *Nat Methods*. 2012;9:676–682.
27. Henderson A. *ParaView Guide, A Parallel Visualization Application*. Clifton Park, NY: Kitware Inc.; 2007.
28. R_Development_Core_Team. *R. A Language and Environment for Statistical Computing*. Vienna, Austria: R Foundation

for Statistical Computing; 2010. Available at: http://www.R-project.org. Accessed October 10, 2011.

29. Balaratnasingam C, Morgan WH, Johnstone V, Pandav SS, Cringle SJ, Yu DY. Histomorphometric measurements in human and dog optic nerve and an estimation of optic nerve pressure gradients in human. *Exp Eye Res*. 2009;89:618–628.
30. Albon J, Farrant S, Akhtar S, et al. Connective tissue structure of the tree shrew optic nerve and associated ageing changes. *Invest Ophthalmol Vis Sci*. 2007;48:2134–2144.
31. Jonas JB, Berenshtein E, Holbach L. Lamina cribrosa thickness and spatial relationships between intraocular space and cerebrospinal fluid space in highly myopic eyes. *Invest Ophthalmol Vis Sci*. 2004;45:2660–2665.
32. Yang H, Downs JC, Bellezza A, Thompson H, Burgoyne CF. 3-D histomorphometry of the normal and early glaucomatous monkey optic nerve head: prelaminar neural tissues and cupping. *Invest Ophthalmol Vis Sci*. 2007;48:5068–5084.
33. Sigal IA, Flanagan JG, Tertinegg I, Ethier CR. 3D morphometry of the human optic nerve head. *Exp Eye Res*. 2010;90:70–80.
34. Burgoyne CF, Downs JC, Bellezza AJ, Suh JK, Hart RT. The optic nerve head as a biomechanical structure: a new paradigm for understanding the role of IOP-related stress and strain in the pathophysiology of glaucomatous optic nerve head damage. *Prog Retin Eye Res*. 2005;24:39–73.
35. Rogers RS, Dharsee M, Ackloo S, Sivak JM, Flanagan JG. Proteomics analyses of human optic nerve head astrocytes following biomechanical strain. *Mol Cell Proteomics*. 2012;11:M111.012302.
36. Hernandez MR. The optic nerve head in glaucoma: role of astrocytes in tissue remodeling. *Prog Retin Eye Res*. 2000;19:297–321.
37. Anderson DR, Hendrickson A. Effect of intraocular pressure on rapid axoplasmic transport in monkey optic nerve. *Invest Ophthalmol*. 1974;13:771.
38. Hiraoka M, Inoue K, Ninomiya T, Takada M. Ischaemia in the Zinn-Haller circle and glaucomatous optic neuropathy in macaque monkeys. *Br J Ophthalmol*. 2012;96:597–603.
39. Liang Y, Fortune B, Cull G, Cioffi GA, Wang L. Quantification of dynamic blood flow autoregulation in optic nerve head of rhesus monkeys. *Exp Eye Res*. 2010;90:203–209.
40. Flammer J, Orgul S, Costa VP, et al. The impact of ocular blood flow in glaucoma. *Prog Retin Eye Res*. 2002;21:359–393.
41. Morrison JC, Johnson EC, Cepurna W, Jia L. Understanding mechanisms of pressure-induced optic nerve damage. *Prog Retin Eye Res*. 2005;24:217–240.
42. Whitmore AV, Libby RT, John SW. Glaucoma: thinking in new ways—a role for autonomous axonal self-destruction and other compartmentalised processes? *Prog Retin Eye Res*. 2005;24:639–662.
43. Sigal IA, Flanagan JG, Tertinegg I, Ethier CR. Modeling individual-specific human optic nerve head biomechanics. Part I: IOP-induced deformations and influence of geometry. *Biomech Model Mechanobiol*. 2009;8:85–98.
44. Bain AC, Meaney DF. Tissue-level thresholds for axonal damage in an experimental model of central nervous system white matter injury. *J Biomech Eng*. 2000;122:615–622.
45. Kirwan RP, Fenerty CH, Crean JK, Wordinger RJ, Clark AF, O'Brien CJ. Influence of cyclical mechanical strain on extracellular matrix gene expression in human lamina cribrosa cells in vitro. *Mol Vis*. 2005;11:798–810.
46. Quill B, Docherty NG, Clark AF, O'Brien CJ. The effect of graded cyclic stretching on extracellular matrix-related gene expression profiles in cultured primary human lamina cribrosa cells. *Invest Ophthalmol Vis Sci*. 2011;52:1908–1915.
47. Wang JH, Thampatty BP. An introductory review of cell mechanobiology. *Biomech Model Mechanobiol*. 2006;5:1–16.
48. Sigal IA, Grimm JL. A few good responses: which mechanical effects of IOP on the ONH to study? *Invest Ophthalmol Vis Sci*. 2012;53:4270–4278.
49. Sigal IA, Yang H, Roberts MD, Burgoyne CF, Downs JC. IOP-induced lamina cribrosa displacement and scleral canal expansion: an analysis of factor interactions using parameterized eye-specific models. *Invest Ophthalmol Vis Sci*. 2011;52:1896–1907.
50. Girard MJ, Downs JC, Bottlang M, Burgoyne CF, Suh JK. Peripapillary and posterior scleral mechanics—part II: experimental and inverse finite element characterization. *J Biomech Eng*. 2009;131(5):051012.
51. Grytz R, Meschke G, Jonas JB. The collagen fibril architecture in the lamina cribrosa and peripapillary sclera predicted by a computational remodeling approach. *Biomech Model Mechanobiol*. 2011;10:371–382.
52. Grytz R, Sigal IA, Ruberti JW, Meschke G, Downs JC. Lamina cribrosa thickening in early glaucoma predicted by a microstructure motivated growth and remodeling approach. *Mech Mater*. 2012;44:99–109.
53. Sander EA, Downs JC, Hart RT, Burgoyne CF, Nauman EA. A cellular solid model of the lamina cribrosa: mechanical dependence on morphology. *J Biomech Eng*. 2006;128:879–889.
54. Coudrillier B, Boote C, Quigley HA, Nguyen TD. Scleral anisotropy and its effects on the mechanical response of the optic nerve head. *Biomech Model Mechanobiol*. 2013;12:941–963.
55. Coudrillier B, Tian J, Alexander S, Myers KM, Quigley HA, Nguyen TD. Biomechanics of the human posterior sclera: age- and glaucoma-related changes measured using inflation testing. *Invest Ophthalmol Vis Sci*. 2012;53:1714–1728.
56. Pijanka JK, Coudrillier B, Ziegler K, et al. Quantitative mapping of collagen fiber orientation in non-glaucoma and glaucoma posterior human sclerae. *Invest Ophthalmol Vis Sci*. 2012;53:5258–5270.
57. Ethier CR, Johnson M, Ruberti J. Ocular biomechanics and biotransport. *Annu Rev Biomed Eng*. 2004;6:249–273.
58. Triyoso DH, Good TA. Pulsatile shear stress leads to DNA fragmentation in human SH-SY5Y neuroblastoma cell line. *J Physiol*. 1999;515:355–365.
59. Ruberti JW, Hallab NJ. Strain-controlled enzymatic cleavage of collagen in loaded matrix. *Biochem Biophys Res Commun*. 2005;336:483–489.
60. Ren R, Jonas JB, Tian G, et al. Cerebrospinal fluid pressure in glaucoma: a prospective study. *Ophthalmology*. 2010;117:259–266.
61. Berdahl JP, Allingham RR, Johnson DH. Cerebrospinal fluid pressure is decreased in primary open-angle glaucoma. *Ophthalmology*. 2008;115:763–768.
62. Sigal IA, Flanagan JG, Tertinegg I, Ethier CR. Modeling individual-specific human optic nerve head biomechanics. Part II: influence of material properties. *Biomech Model Mechanobiol*. 2009;8:99–109.
63. Yang H, Downs JC, Sigal IA, Roberts MD, Thompson H, Burgoyne CF. Deformation of the normal monkey optic nerve head connective tissue after acute IOP elevation within 3-D histomorphometric reconstructions. *Invest Ophthalmol Vis Sci*. 2009;50:5785–5799.
64. Sigal IA, Bilonick RA, Kagemann L, et al. The optic nerve head as a robust biomechanical system. *Invest Ophthalmol Vis Sci*. 2012;53:2658–2667.
65. Ren R, Wang N, Li B, et al. Lamina cribrosa and peripapillary sclera histomorphometry in normal and advanced glaucomatous Chinese eyes with various axial length. *Invest Ophthalmol Vis Sci*. 2009;50:2175–2184.

Investigative Ophthalmology & Visual Science

66. Kiumehr S, Park SC, Syril D, et al. In vivo evaluation of focal lamina cribrosa defects in glaucoma. *Arch Ophthalmol*. 2012; 130:552–559.
67. Strouthidis NG, Fortune B, Yang H, Sigal IA, Burgoyne CF. The effect of acute intraocular pressure elevation on the monkey optic nerve head as detected by spectral domain optical coherence tomography. *Invest Ophthalmol Vis Sci*. 2011;52: 9431–9437.
68. Girard MJ, Strouthidis NG, Ethier CR, Mari JM. Shadow removal and contrast enhancement in optical coherence tomography images of the human optic nerve head. *Invest Ophthalmol Vis Sci*. 2011; 52:7738–7748.
69. Kagemann L, Ishikawa H, Wollstein G, et al. Ultrahigh-resolution spectral domain optical coherence tomography imaging of the lamina cribrosa. *Ophthalmic Surg Lasers Imaging*. 2008;39:S126–S131.
70. Yan D, McPheeters S, Johnson G, Utzinger U, Vande Geest JP. Microstructural differences in the human posterior sclera as a function of age and race. *Invest Ophthalmol Vis Sci*. 2011;52: 821–829.
71. Roberts MD, Liang Y, Sigal IA, et al. Correlation between local stress and strain and lamina cribrosa connective tissue volume fraction in normal monkey eyes. *Invest Ophthalmol Vis Sci*. 2010;51:295–307.
72. Girard M, Suh JK, Hart RT, Burgoyne CF, Downs JC. Effects of storage time on the mechanical properties of rabbit peripapillary sclera after enucleation. *Curr Eye Res*. 2007;32:465–470.
73. Jonas JB, Berenshtein E, Holbach L. Anatomic relationship between lamina cribrosa, intraocular space, and cerebrospinal fluid space. *Invest Ophthalmol Vis Sci*. 2003;44:5189–5195.
74. Quigley EN, Quigley HA, Pease ME, Kerrigan LA. Quantitative studies of elastin in the optic nerve heads of persons with primary open-angle glaucoma. *Ophthalmology*. 1996;103: 1680–1685.
75. Oyama T, Abe H, Ushiki T. The connective tissue and glial framework in the optic nerve head of the normal human eye: light and scanning electron microscopic studies. *Arch Histol Cytol*. 2006;69:341–356.
76. Yang H, Williams G, Downs JC, et al. Posterior (outward) migration of the lamina cribrosa and early cupping in monkey experimental glaucoma. *Invest Ophthalmol Vis Sci*. 2011;52: 7109–7121.
77. Sigal IA, Flanagan JG, Lathrop KL, Tertinegg I, Bilonick R. Human lamina cribrosa insertion and age. *Invest Ophthalmol Vis Sci*. 2012;53:6870–6879.
78. Crawford Downs J, Roberts MD, Sigal IA. Glaucomatous cupping of the lamina cribrosa: a review of the evidence for active progressive remodeling as a mechanism. *Exp Eye Res*. 2011;93:133–140.
79. Girard MJ, Strouthidis NG, Desjardins A, Mari JM, Ethier CR. In vivo optic nerve head biomechanics: performance testing of a 3D tracking algorithm. *J R Soc Interface*. 2013;10(87): 20130459.
80. Strouthidis NG, Grimm J, Williams GA, Cull GA, Wilson DJ, Burgoyne CF. A comparison of optic nerve head morphology viewed by spectral domain optical coherence tomography and by serial histology. *Invest Ophthalmol Vis Sci*. 2010;51:1464–1474.
81. Sigal IA, Yang H, Roberts MD, Downs JC. Morphing methods to parameterize specimen-specific finite element model geometries. *J Biomech*. 2010;43:254–262.

Appendix

The similarity measure was the normalized cross-correlation function:

$$\boldsymbol{\Pi}_{\sim} = \frac{\sum_{X_i \in \Theta(X)} F(X_i) M\left(X_i + \vec{\boldsymbol{u}}(X)\right)}{\sqrt{\sum_{X_i \in \Theta(X)} F^2(X_i) \sum_{X_i \in \Theta(X)} M^2\left(X_i + \vec{\boldsymbol{u}}(X)\right)}}$$

where $\Theta(\boldsymbol{X})$ is the neighborhood of a point $\boldsymbol{X}$ at which the similarity is being computed, F and M are the fixed (target) and moving (deforming) images, respectively, and $\vec{\boldsymbol{u}}$ is the displacement field.

In the image registration process we seek $\vec{\boldsymbol{u}}$ that minimizes the potential energy $\boldsymbol{\Pi}$ over the domain Ω, as given by:

$$\boldsymbol{\Pi} = \boldsymbol{\Pi}_R - \boldsymbol{\Pi}_{\sim}$$

where $\boldsymbol{\Pi}_{\sim}$ is defined as above, and

$$\boldsymbol{\Pi}_R = \int_{\Omega} (\boldsymbol{\sigma} : \varepsilon) d\Omega$$

The stress ($\boldsymbol{\sigma}$) and strain ($\boldsymbol{\varepsilon}$) are related by $\boldsymbol{\sigma}_{ij} = \boldsymbol{C}_{ijkl}\boldsymbol{\varepsilon}_{kl}$. The tensor $\boldsymbol{C}$ reduces to two coefficients with the simplified materials we assume. The forces guiding the registration (the loads) can be computed with:

$$\vec{F}_{\sim} = \nabla \boldsymbol{\Pi}_{\sim}$$

The process of registration proceeds until the potential energy is minimized (at least in a local minimum). In our implementation, the potential energy is minimized with respect to the baseline image (the undeformed configuration), $\boldsymbol{X}$ for each time step.

Investigative Ophthalmology & Visual Science